International Journal of Heat and Mass Transfer 52 (2009) 5479–5495

Contents lists available at ScienceDirect

International Journal of Heat and Mass Transfer

journal homepage: www.elsevier.com/locate/ijhmt

Measurements of jet flows impinging into a channel containing a rod bundle using dynamic PIV

Noushin Amini [a], Yassin A. Hassan [b,*]

[a] *Department of Mechanical Engineering, Texas A&M University, College Station, TX 77843-3123, USA*
[b] *Department of Nuclear Engineering, Texas A&M University, College Station, TX 77843-3133, USA*

ARTICLE INFO

Article history:
Received 23 October 2008
Received in revised form 3 July 2009
Available online 13 August 2009

Keywords:
PIV
MIR technique
Rod bundle
Impinging jets

ABSTRACT

In this investigation, full-field velocity profiles of jet flows impinging into a rod bundle were measured using Particle Image Velocimetry (PIV) technique in a facility with Matched-Index of Refraction. The test section consisted of a 1 m long rectangular channel with a cross-sectional area of 76.2×76.2 mm^2. Water was pumped through either single or double jets located on the top wall of the channel. The Reynolds numbers of the inlet jets were varied from 4470 to 13,400. Inside the channel adjacent to the inlet jets, a rod bundle was configured with 29 staggered tubes of 10.67 mm outside diameter (O.D.). The time-resolved velocity fields were obtained for regions within the rod bundle from which the vorticity fields and the turbulent characteristics of those regions were calculated. The results are useful for developing new models to help predict the flow patterns in the lower plenum of Gas Cooled Reactors.

1. Introduction

The proposed development of the Next Generation Nuclear Plants (NGNPs) holds great promise as a viable solution to burgeoning global energy needs. The NGNP has the opportunity to ensure the sustainability of nuclear energy through its efforts to improve the fuel cycle, reprocessing and fuel treatment. The Very High Temperature Reactor (VHTR) is one of the six designs proposed to meet the needs of the Generation-IV reactors because of its high efficiency in electricity production [1]. However, development of the VHTR systems, and other advanced systems, will require the enhancement of current – and development of new – predictive methods utilized to model the phenomena associated with a nuclear power production plant. Particularly, modeling system's thermal hydraulic behavior is essential to the development of predictive methods for performance studies of new reactor designs. Therefore, the study of flow structure within the core of a VHTR, whether a prismatic block or a pebble-bed core, is of great importance. In the present study, investigations were conducted to study physical phenomena expected in a prismatic core NGNP, especially the flow of high temperature helium coolant jets exiting the core and entering the lower plenum of the core (core bottom structure). Some of the important phenomena occurring in the lower plenum are how the coolant flow is hitting the lower plenum bottom surface, the interaction between the circular coolant jet flows and the neighboring circular graphite support rods of the lower plenum and the surrounding walls, as well as the distribution and the degree of mixing of the high temperature helium coolant flows with the lower plenum flows. Experimental characterizations of the flow behavior in this system are an essential element in the efforts to develop models capable of accurately predicting plant's thermal hydraulic behavior. To understand these phenomena and to measure the flow characteristics in the lower plenum, many experiments have investigated single or dual jets effusing into flat plates or rod bundles.

One of the early investigations was performed by Donaldson and Snedeker [2] and Donaldson et al. [3] who presented the mean flow characteristics and the heat transfer rates of a circular convergent nozzle jet impinging on plates of different shapes at different angles. Additionally, the turbulent characteristics and the heat transfer rates of a circular subsonic jet effusing normally to a flat plate were studied. Landreth and Adrian [4] used Particle Image Velocimetry (PIV) techniques to obtain the instantaneous and average velocity fields of a circular water jet which was connected to a converging nozzle at its end and was impinging vertically on a flat plate. They used the instantaneous velocity fields to calculate the vorticity and shear stress rate. In another study, Cooper et al. [5] investigated flow from a turbulent jet impinging orthogonally upon a large plane surface. In this experiment both the jet discharge velocities and the jet outlet height above the plate were varied. Such efforts allowed analysis of the mean velocity profile in the vicinity of the plate surface as well as each component of the Reynolds stress exerted on the plate for a variety of flow conditions. Nishino et al. [6] implemented 2D and 3D Particle Tracking Velocimetry (PTV) technique to analyze the turbulence statistics in

---

* Corresponding author. Tel.: +1 979 845 7090.
E-mail address: y-hassan@tamu.edu (Y.A. Hassan).

0017-9310/$ - see front matter © 2009 Elsevier Ltd. All rights reserved.
doi:10.1016/j.ijheatmasstransfer.2009.07.002

the stagnation region of a fixed Reynolds number jet which was impinging normally on a flat plate. Sakakibara et al. [7] obtained measurements of simultaneous velocity and temperature profiles in the stagnation region of an impinging plane jet using both digital PIV and Laser-Induced Fluorescence (LIF). Moreover, Mi et al. [8] investigated the effects of jet exit conditions on the passive scalar field by using two types of nozzles at a fixed Reynolds number; a smooth converging nozzle and a long straight pipe. They obtained the jet scalar field and the flow structure of each jet and showed that their experimental results corresponded well to the analytical results. In the investigation done by Alekseenko et al. [9], stereo and 2D PIV techniques were applied to study the flow characteristics of a jet impinging on a flat plate with varying swirl rates for a fixed Reynolds number of 8900. They observed that the decay rate of the absolute velocity of the non-swirling jets is less than that of the swirling jets. Abdel-Fattah [10] numerically and experimentally studied the case of two circular air jets impinging on a flat plate with no cross-flow in two dimensions. He investigated the effects of the Reynolds number, nozzle to plate spacing, nozzle to nozzle centerline spacing and the jet angle on the creation of a sub-atmospheric region between the two jets.

Aside from experiments concerned only with the behavior of jets impinging on flat plates, flow mixing phenomena, including the velocity fields associated with impinging jets within rod bundles, have frequently been studied experimentally. The flow structure within the rod bundles is of great interest among nuclear reactor engineers because of the special configuration of the fuel rods in a nuclear reactor core. In an investigation performed by Trupp and Azad [11], the mean velocity and turbulent characteristics of the axial flow within a triangular rod bundle were measured for different Reynolds numbers and different tube spacings. Hooper and Wood [12] obtained the mean axial velocity, wall shear stress, and all six Reynolds stresses with varied Reynolds numbers for a fixed pitch squared bundle consisting of six rods. Hooper and Rehme [13] and Rehme [14] used hot-wire anemometry to measure the turbulence intensities of flow through a rod bundle in a rectangular channel. In the former experiment, they used two geometries, one containing four rods and the other one having six rods, while in the latter the bundle consisted of four rods. Renksizbulut and Hadaller [15] used Laser-Doppler Anemometry (LDA) to obtain the mean velocity and turbulent flow characteristics at a fixed Reynolds number within a square channel of six rods. Additionally, Smith et al. [16] performed thermal hydraulic experiments in a 5×5 rod bundle with a heated rod using a PIV system. Subsequent Computational Fluid Dynamics (CFD) simulations were also performed to develop confidence in the use of CFD as a tool to investigate the flow and temperature distributions in a rod bundle array with spacer grids. In an effort to examine the lateral flow structure of a square sub-channel geometry, Chang et al. [17] used two-dimensional LDA to measure detailed turbulent flow profiles on a 5×5 rod bundle array. Notably, the study of impinging jets is not limited to nuclear industry. There are many other applications of impinging jets such as cooling electronic components or gas turbine blades, annealing of metals and drying of textiles, paper and hard wood. One example of research for different applications of impinging jets was demonstrated in Velasco et al.'s [18] investigation. They carried out a 2D PIV measurement to obtain the gas flow behavior in the space between the breach and neighbor tubes of a shell-and-tube heat exchanger for a range of Reynolds number from 0.8×10^5 to 2.7×10^5. They showed that increasing the gas Reynolds number improves the jet penetration and turbulence intensity level close to the breach. They observed that the presence of the tubes distorts the jet shape.

McEligot and McCreery [19] and McCreery and Condie [20] emphasized the need for performing benchmark experiments and investigating the combined effects of the lower plenum flows for the purpose of developing effective models in such systems. They also asserted that the development of CFD codes to model flow in the lower plenum of a conceptual VHTR should be in concert with carrying out the experimental investigations over a wide range of operating conditions. These estimates predicted Reynolds numbers for jets exhausting into the lower plenum to vary from 50,000, at full-power operation, to as low as 5000, under partial loading conditions. Such large variations in flow parameters require that prediction methods anticipate and consider the mechanisms which control fluid flow behavior under different operating conditions.

In the current study, measurements of full-field velocity profiles of jet flow in a rod bundle were obtained through the use of Particle Image Velocimetry (PIV) and Matched-Index of Refraction (MIR) techniques. These measurements allowed identification of the important parameters of flow behavior. These efforts will help in the development of the predictive methods utilized in analysis of the VHTR systems by aiding in the development of experimental databases, and providing benchmark data for CFD codes.

2. Experimental methodology

2.1. Geometry and flow configuration

In this investigation, experimental studies of flow behavior in the lower plenum of a conceptual VHTR have been conducted. The experimental facility consisted of a hydraulic loop equipped with a submergible pump which would drive the water flow into two separate loops each leading to one of the inlet jets of the channel. The separate loops had flowmeters (Blue-White Industries, accuracy ±5%) indicating the flow rates of each loop for determining mean flow velocity in each inlet jet. Both of the inlet jets entered the channel top wall at an angle of 90°. The channel had a rectangular cross section with the dimensions of $L = 1016$ mm, $H = 76.2$ mm and $W = 76.2$ mm. The channel had a single outlet located at one of its ends. In order to ensure good visual conditions for PIV measurements, the channel was constructed with transparent polycarbonate sheets. To have uniform flow, two flow straighteners are installed close to the two ends of the channel. The experimental set-up developed to model this conceptual system is depicted in Fig. 1.

As it is shown in Fig. 1, the rod bundle consisted of 29 tubes fixed to the upper and lower surfaces of the channel. These tubes possessed a 10.67 mm outer diameter and a 10.16 mm inner diameter and were set as "in-line" in z direction, each row of tube is exactly placed behind the next row, with 19 mm pitch and as "staggered" in x direction, each row of tubes is displaced with regards to the previous row, with 25.4 mm pitch (Fig. 2).

The inlet jets were fixed 1 cm from the top wall of the channel. It should be noted that the inlet jets were made of the same tubes as the rod bundle. In this study, the Reynolds number is calculated as shown in Eq. (1), where U_{jet} is the inlet jet's mean velocity, d is the inlet jet's inner diameter, ρ is water density and μ is water dynamic viscosity both at room's temperature.

$$\mathrm{Re}_{\text{jet}} = \frac{\rho U_{\text{jet}} d}{\mu} \tag{1}$$

Matched-Index of Refraction (MIR) technique was used in the development of the experimental test facility to allow a more complete investigation of flow behavior to be executed. The material used for the rod bundle tubes and the inlet jets had the same index of refraction as water which was the working fluid in the experiment. Using the MIR technique allowed for complete visualization of the flow in the interior regions of the

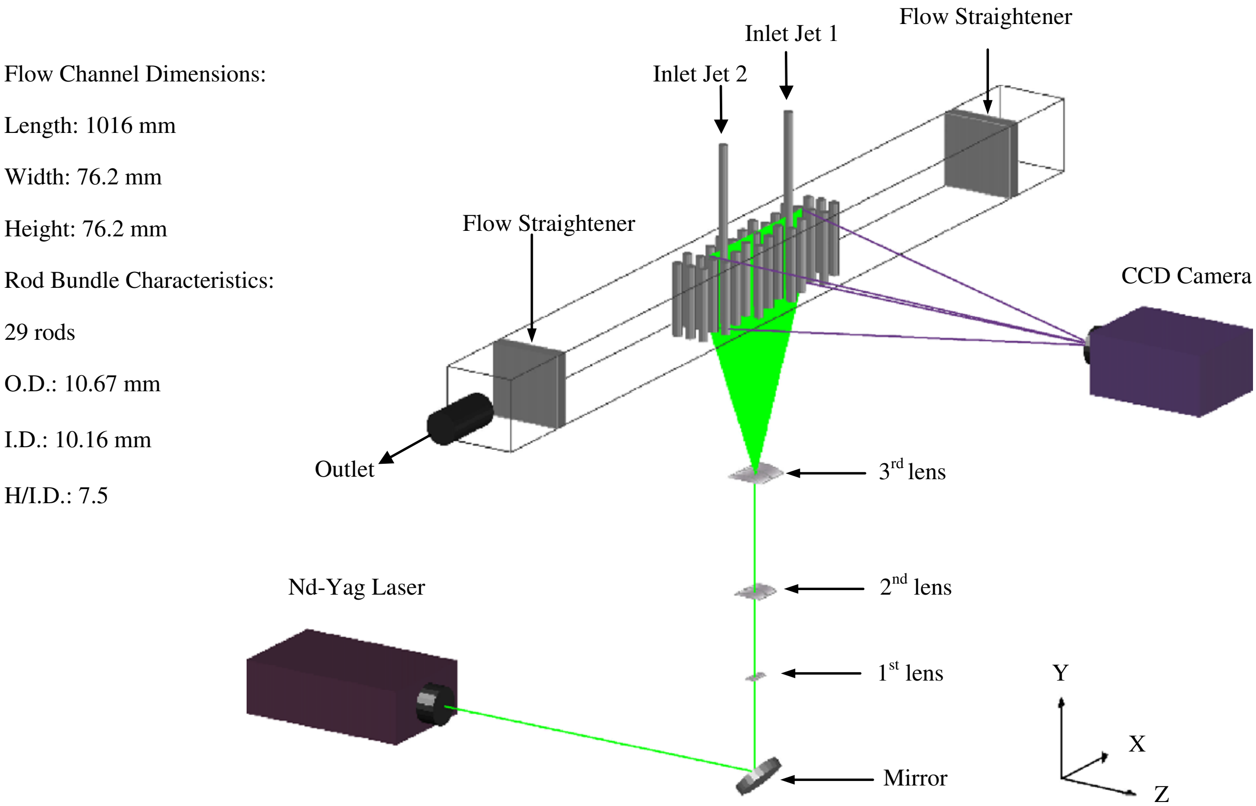

Fig. 1. Test section schematic.

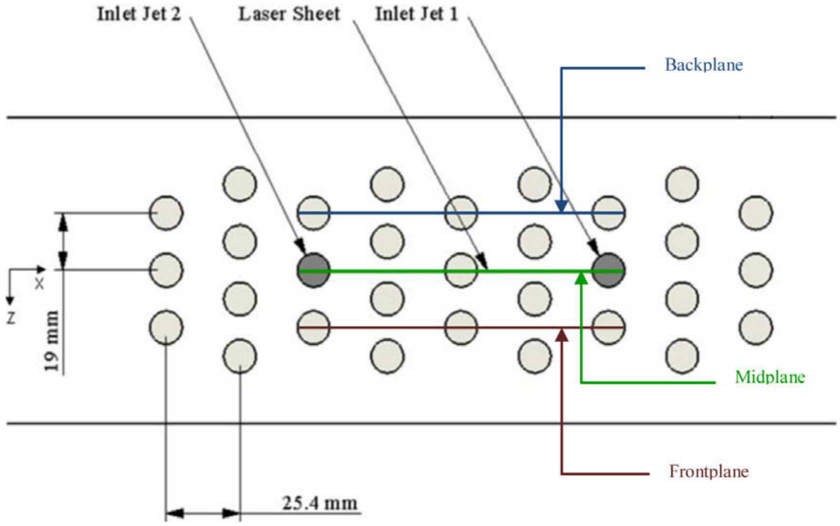

Fig. 2. Schematic of the channel top wall showing the two inlet jets and the measurement planes.

bundle. Since the rods were represented as hollow cylinders, water filled the tubes to avoid optical aberrations. Such an approach allows complete visualization of the flow without hidden regions obstructed by the presence of the rods. Moreover, a variety of flow conditions were developed in response to cursory investigations suggesting the possibility of large variations in reactor operating conditions. The matrix characterizing the flow conditions used in experimental investigations is presented in Table 1 to demonstrate the range over which parameters were

Table 1
Experimental matrix of variation of parameters, $Re_{jet\ 1}$ is the first jet's Reynolds number and $Re_{jet\ 2}$ is the second jet's Reynolds number.

	$Re_{jet\ 1}$	$Re_{jet\ 2}$
Single jet	13,400 4470	– –
Dual jets	11,160	6250

evaluated during this investigation. Relevant characteristics of the Particle Image Velocimetry (PIV) and MIR systems, which are developed for this experiment, will be discussed separately in the following sections.

2.2. Matched-Index of Refraction (MIR) technique

In the design of the test section (see Fig. 1), MIR principles were employed to enhance the capability of the experimental investigations to characterize flow behavior inside the rod bundle without having the effect of the rods obstructing the view. The flow channel was constructed with transparent polycarbonate sheets to allow both the passage of the illuminating laser sheets and the acquisition of PIV images. Although Polycarbonate does not exhibit the same refractive index as water, since it only comprises the outer surface of the channel, it does not affect imaging inside the channel. Thus, MIR techniques were used in the selection of a material to simulate rods. Fluorinated ethylene–propylene (FEP) tubes were selected for the rod material since this material possessed an index of refraction nearly identical to that of water; consequently, it does not produce any optical distortion. The refractive index (or index of refraction) of a material is the factor showing how much the speed of light or other electromagnetic waves is reduced in that material. The refractive index of a medium (n) is given as the ratio of the electromagnetic wave velocity (c) in the medium to the velocity of the electromagnetic wave in a reference medium (v) such as vacuum.

$$n = \frac{c}{v} \tag{2}$$

The list of the refractive indices for many materials is available now but it should be noted that the refractive index of a material is affected by many factors among which the light frequency is one of the most important ones. The refractive index of water is 1.333 at a light wavelength of 589 nm [21]. As the laser light frequency and the water temperature were kept constant in this experiment, it was assumed that the refractive index of water remained constant.

In total, 29 tubes were fixed to the upper and lower surfaces of the test section, near the two inlet jets located on the upper surface of the facility, to simulate the presence of a rod bundle in the jet exhaustion area. It is important to note that FEP tubes were filled with water. This measure was necessary to maintain a constant index of refraction throughout the test facility and to reduce the noise due to laser light reflection and refraction at the interior rod interface. The effect of MIR technique can be distinctly observed when visualizing partially submerged tubes as seen in Fig. 3. Such measures allow flow behavior to be assessed throughout the channel volume by significantly reducing undesirable reflection and refraction and, effectively eliminating the blockage of interior regions by rod structures.

2.3. Particle Image Velocimetry (PIV)

In this study, a 2D Particle Image Velocimetry (PIV) technique was used to measure the flow field. PIV is a valuable flow visualization technique used to measure the flow velocity since full-field velocity measurements can be obtained without disturbing the flow (i.e. non-intrusive). In PIV, the motion of particles (i.e. tracers) within a fluid, are tracked to ascertain the motion of the fluid itself. Since it must be assumed that tracers' motion is determined by that of the fluid, tracer particles must faithfully follow the fluid flow for accurate full-field velocity profiles to be obtained [22]. In general, these tracer particles may be naturally occurring impurities or manufactured seeds added to the fluid prior to the experiment. In the present investigation, the fluid was seeded with Expancel 091 UD particles with diameters in the range of 6–9 μm and specific gravity of 1.05. These tracer particles were specifically chosen because their material density is close to that of water, which assures the tracer particle motion best reflects the actual flow path. Another superior feature of PIV technique is the ability to measure full-field velocity components. The principles of PIV technique have been explained by Adrian [23], Hassan et al. [24,25], and the development and progression of this technique is described by Adrian [26].

The PIV system consists of several sub-systems including a high power laser which is used as the illumination source, an optical set-up which consists of a number of lenses to turn the laser light into a laser sheet, and a high speed camera capturing images of the illuminated plane. The seeding particles in the fluid scatter the laser light which is captured by the video acquisition system. In the current experiment, a Nd-Yag laser (New Wave Research, Pegasus PIV, wavelength of 527 nm, maximum energy of 20 mJ per pulse), served as the illumination source for the PIV system. Illumination from this source was manipulated through the appropriate use of optical instruments (a mirror and three cylindrical lenses) to produce a laser sheet of 1 mm thickness on the channel's bottom wall. This allowed the illumination of planes parallel to the vertical axis. A high speed/high resolution CCD camera (Vision Research, Phantom v7.3, 800 × 600 pixels, 12 bit) captured images of the illuminated PIV particles at a rate of 1000 frames per second (fps). With that frame rate, 5000 images are acquired over a period of 5 seconds which is similar to the measurement duration in the experiment done by Kim et al. [27]. In the present experiment, the range of the jet's Reynolds numbers are in the turbulent flow region (the range of the Reynolds numbers are up to ten times

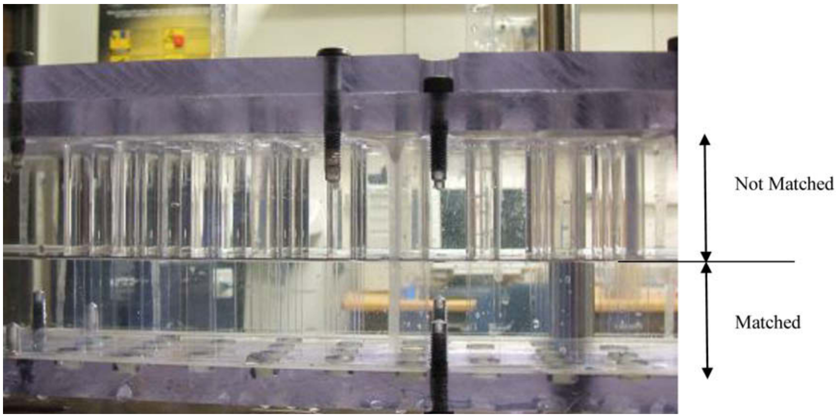

Fig. 3. Picture of the experimental set-up illustrating the MIR technique with channel which is half filled.

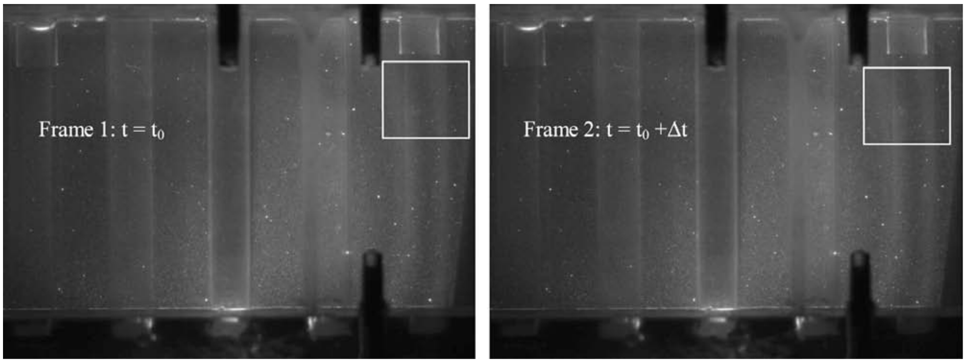

Fig. 4. Two subsequent images illustrating the cross-correlation technique.

higher than the jets in Kim et al.'s experiment), therefore higher frequency and smaller time scale flow patterns are more expected in comparison with Kim et al.'s study. Consequently, such a high frame rate (1000 frame per second) is chosen to enable the capture of the higher frequency flow structures.

The camera was oriented perpendicular to the laser sheet direction to acquire video data depicting fluid behavior in the illuminated planes. A system of automatic and manual translation mechanisms were utilized to synchronize the laser plane of illumination with camera focal planes to allow movement of the measuring area within the measuring volume in z direction. This allowed flow behavior to be evaluated in three different planes parallel to the vertical axis (Fig. 2).

In PIV, to measure the velocity, two consecutive recorded images are compared at subregion level through signal processing methods such as cross-correlation technique and the particles displacement vectors are obtained subsequently. According to Hassan et al. [24,25], the binary cross-correlation coefficient, C_{ij}, between candidate spot pairs in frames 1 and 2 of Fig. 4 is given by

$$C_{ij} = \frac{\sum_{y,x=1}^{L} F_1^b \cap F_2^b}{\sqrt{(B_1 \times B_2)}} \tag{3}$$

where the numerator is the sum of the logical products between the corresponding pixels in the subregions of frames 1 and 2 (F_1^b and F_2^b being the binary pixel values in frames 1 and 2, respectively, and L being the size of the subregions), and B_1 and B_2 show the total number of pixels of binary value 1 in the subregions in frames 1 and 2. It should be noted that during the post-processing, the size of the subregions was adjusted for each case depending on the Reynolds number and the number of impinging jets.

In this experiment, the CCD camera captured 5000 images for each plane in each case. Then, the acquired data were analyzed through the use of appropriate image processing and PIV analysis techniques. The forementioned cross-correlation algorithm was applied to the captured images through the use of a software specifically written for the analysis of the PIV images [28]. The results were filtered to remove the erroneous vectors. The final results were imported to TecPlot for visualization and analysis.

2.3.1. PIV Error analysis

Considering the accuracy of PIV, a few different sources contribute to PIV measurement error. First, the experimental set-up and the optical instrument imperfections should be considered such as the flowmeter errors which is ±5% and optical errors due to laser sheet misalignment. The second type of possible error is attributed to the seeding particles, specifically regarding their sizes and how faithfully those particles follow the fluid motion. By choosing seeding particles with a density close to water (specific gravity of 1.05); the particles are expected to follow the fluid motion very well.

Another source of error could be the limited sample size. The mean flow characteristics are calculated by post-processing the PIV images. If the number of images or the sample size is not high enough, an error would be caused as a result of averaging insufficient number of images. In this experiment, 5000 images have been captured for each set of measurements. To ensure the adequacy of this procedure, the results of averaging 5000 images were compared to those of 100, 200, ... , 500, 1000, ... , 4500 images of the midplane of the test section. Fig. 5 shows the deviation in the velocity magnitudes of different sample sizes from that of 5000 images for the case of single impinging jet with $\mathrm{Re_{jet\ 1}} = 13{,}400$. As seen in Fig. 5, the smaller the sample size is, the higher the difference is between the obtained velocity magnitudes from the velocity magnitude calculated by averaging 5000 images. Fig. 5 represents that the sample size error tends to decrease as the number of images increases. The error goes from 11.8% for 100 images down to 0.45% for 4500 images. The same trend was observed for all of the other cases; therefore, to have the highest possible accuracy, each test condition was evaluated with 5000 images.

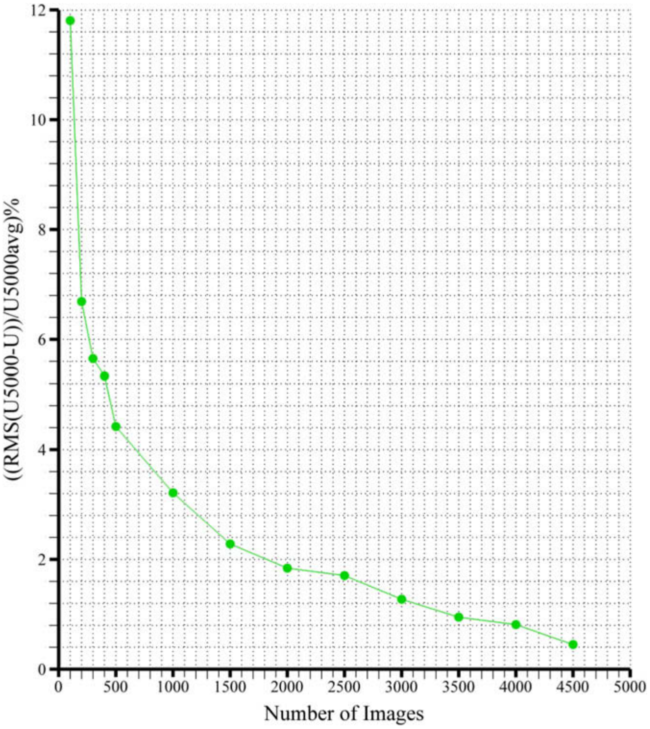

Fig. 5. Effect of sample size on the accuracy of measured velocity magnitudes when compared to a sample of 5000 images. Data obtained for the case of single isothermal inlet jet with $\mathrm{Re_{jet\ 1}} = 13{,}400$.

Table 2
Characteristics of the synthetic images used for error analysis.

Image size	256 × 256 pixel
Area	4×4 cm^2
Laser thickness	2 mm
Interval	0.005 s
Maximum velocity	10 pixel/interval

An additional source of error arises from the post-processing software's error in analyzing the PIV images. The accuracy of the post-processing software was tested using synthetic images of a 3D shear jet flow obtained from the PIV Standard Image website [29]. The characteristics of the synthetic images used for these tests are shown in Table 2. The results indicated that the error of the post-processing software is of subpixel order which is 0.629 pixel/(time interval) for particles moving with the maximum velocity of 10 pixels/(time interval).

3. Results

As mentioned earlier, experiments were carried out for several cases with both single and dual jets impinging into the rod bundle with varied Reynolds numbers. For clarity, the results for each condition are presented separately in the following subsections.

3.1. Single jet

In this case, a single inlet jet (Inlet Jet 1) injected the working fluid into the channel. The time-averaged velocity fields were obtained at three discrete planes throughout the interrogation domain for each of the selected inlet jet Reynolds numbers. Fig. 6 depicts the average velocity fields obtained for a single isothermal inlet jet discharging into the midplane for two different Reynolds numbers. The white lines in the figure represent the streamtraces calculated by means of TecPlot which help to identify flow structure. The velocity vectors are shown in black and are overlaid on a contour map which describes the *Y*-velocity component.

As seen in Fig. 6(a) and (b), a discontinuity is observed in the upper section of the jets' velocity profiles. This can be attributed to undesired laser reflections at these locations. The data obtained for those regions was omitted, since it had no effect on the rest of the results. It is possible to interpolate the data during post-processing and obtain the velocity profile in the excluded regions; however to maintain the integrity of the raw data, no data interpolation, approximation, or smoothing was performed.

Both of the plots in Fig. 6 show a well-defined radial velocity gradient, with the maximum velocity at the jet's core and decreasing velocity in radial direction. In both cases the streamtraces on both sides of the jet are seen to shift toward the jet. Additionally, the higher Reynolds number jet (Fig. 6(a)), the jet maintains its

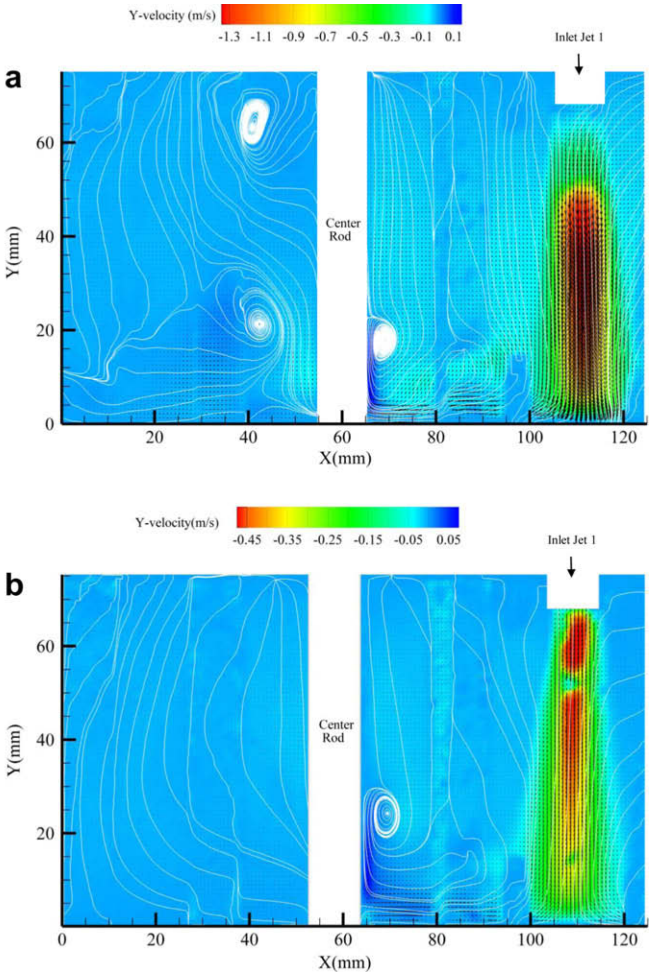

Fig. 6. Time-averaged velocity field, the contour plot of the *Y*-velocity component and the streamtraces along the vertical midplane for a single isothermal inlet jet with (a) $\mathrm{Re}_{\mathrm{jet}\ 1} = 13{,}400$ and (b) $\mathrm{Re}_{\mathrm{jet}\ 1} = 4470$.

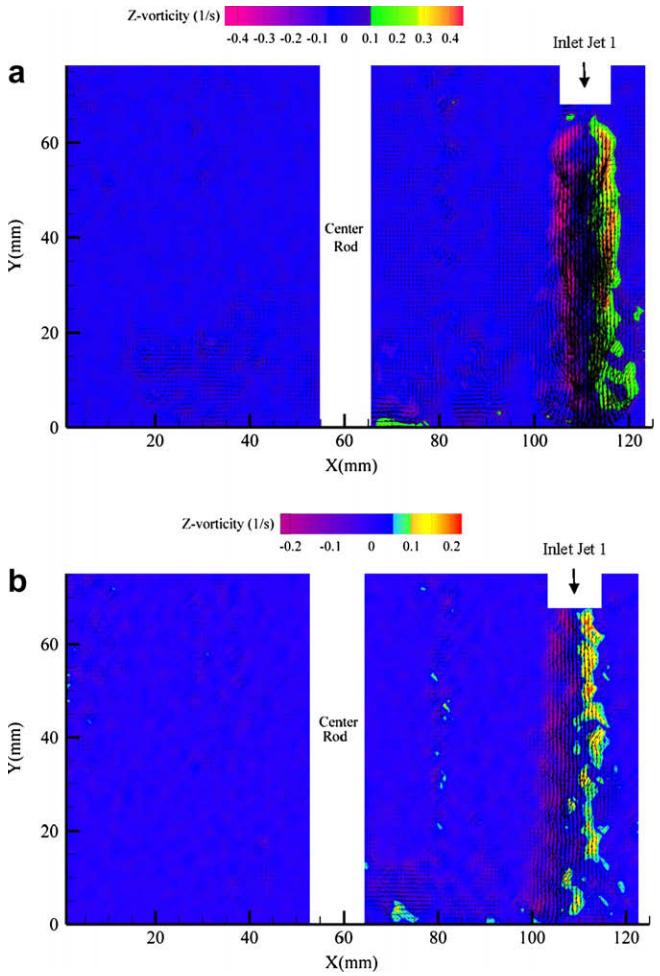

Fig. 7. Instantaneous velocity vectors overlaid on a contour map of *Z*-vorticity along the vertical midplane for a single isothermal inlet jet with (a) $\mathrm{Re}_{\mathrm{jet}\ 1} = 13{,}400$ and (b) $\mathrm{Re}_{\mathrm{jet}\ 1} = 4470$.

highest velocity core further into the channel than the lower Reynolds number jet (Fig. 6(b)).

In both cases a recirculation zone is identified on the right-hand side of the center rod; however, the size and the location of these recirculation zones are different from one case to another. In the higher Reynolds case, the recirculation zone appears at a lower height and closer to the center rod and displays a stronger recirculation than the lower Reynolds number jet. In Fig. 6(a), there are two other recirculation zones observed on the left-hand side of the center rod which are not present in Fig. 6(b). The time-averaged velocity fields for the impinging jets with the same Reynolds numbers are presented in a paper by Amini et al. [30] although it should be mentioned that those velocity fields are obtained by averaging over 500 images. It is seen that for each of the cases, the recirculation zone on the right-hand side of the center rod is identified either by averaging over 500 images or by averaging over 5000 images. However, a significant difference is observed in the number and the size of the recirculation zones observed on the left-hand side of the center rod as a result of the sample size. When averaging 5000 images, the two key recirculation zones previously mentioned are present on the left-hand side of the center rod, but when the velocity field is obtained by averaging 500 images, three small vortices appear in the same region.

In Fig. 7, the instantaneous velocity vectors are presented with the vorticity fields for a single impinging jet with Reynolds numbers of 13,400 and 4470. As shown in Fig. 7, in both cases, vortex structures with opposite directions are seen in the outer regions of the impinging jets. The opposite directions of the vortices are shown by positive and negative values in this figure. It should be noted that vortex structures have scarcely been identified in the center region of the jet. Expectedly, the magnitude of the vorticity is noticeably higher for the higher Reynolds number jet. The presence of the vortices in the outer regions of the jets explains the shift of the streamtraces toward the jet in Fig. 6. More simply, the jets entrain some of the channel flow while injecting into the channel. In Fig. 7(a), the vorticity pattern in the opposite outer regions of the jet is more intense and exhibits symmetry. Alternatively, in Fig. 7(b), the vortex structures are more scattered and non-symmetrical.

To have a better understanding of the jet flow behavior and the velocity changes in the vertical direction, lineprobes of the Y-velocity component and X-velocity component were obtained at three different heights of the channel's midplane. These results are presented in Figs. 8 and 9, respectively. In each of the figures, the Y-velocity magnitude and X-velocity magnitude are normalized by the inlet jet's mean velocity obtained from flowmeter readings. Additionally, the horizontal distance is normalized by the inlet jet's inner diameter.

In Fig. 8, for both cases the highest measured velocity is happening at 40 mm above the bottom surface of the channel and a positive velocity is observed near the center rod at 20 mm above the bottom surface where the key recirculation zone is happening. In Fig. 8(a), lineprobes of $Y = 40$ mm and $Y = 30$ mm match well with each other in the region where the jet impinges and the lineprobe of $Y = 20$ mm shows a maximum velocity at the center of the jet which is lower than the maximum velocity of the other two lineprobes at the same region showing that the jet's maximum velocity decreases as it gets closer to the bottom surface of the channel. It is also seen that there is a minor fluctuation in the Y-velocity lineprobes of $Y = 30$ mm and $Y = 20$ mm on the left-hand

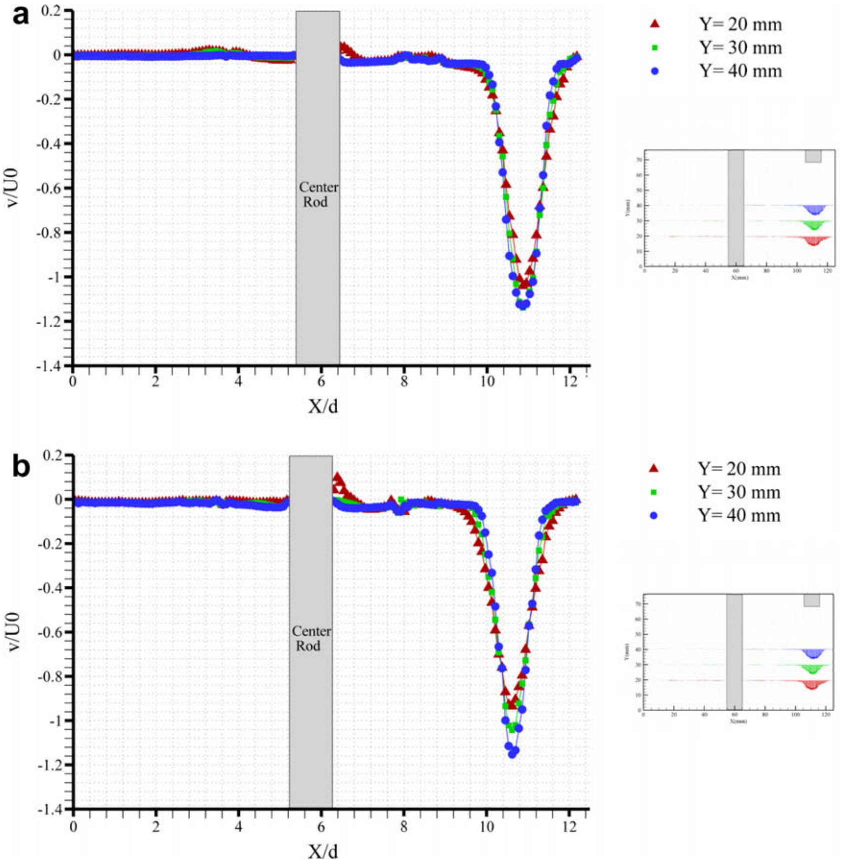

Fig. 8. Normalized Y-velocity component plot along a lineprobe at different heights of the channel's midplane for a single isothermal inlet jet with (a) $\mathrm{Re}_{\mathrm{jet}\ 1} = 13{,}400$ and (b) $\mathrm{Re}_{\mathrm{jet}\ 1} = 4470$.

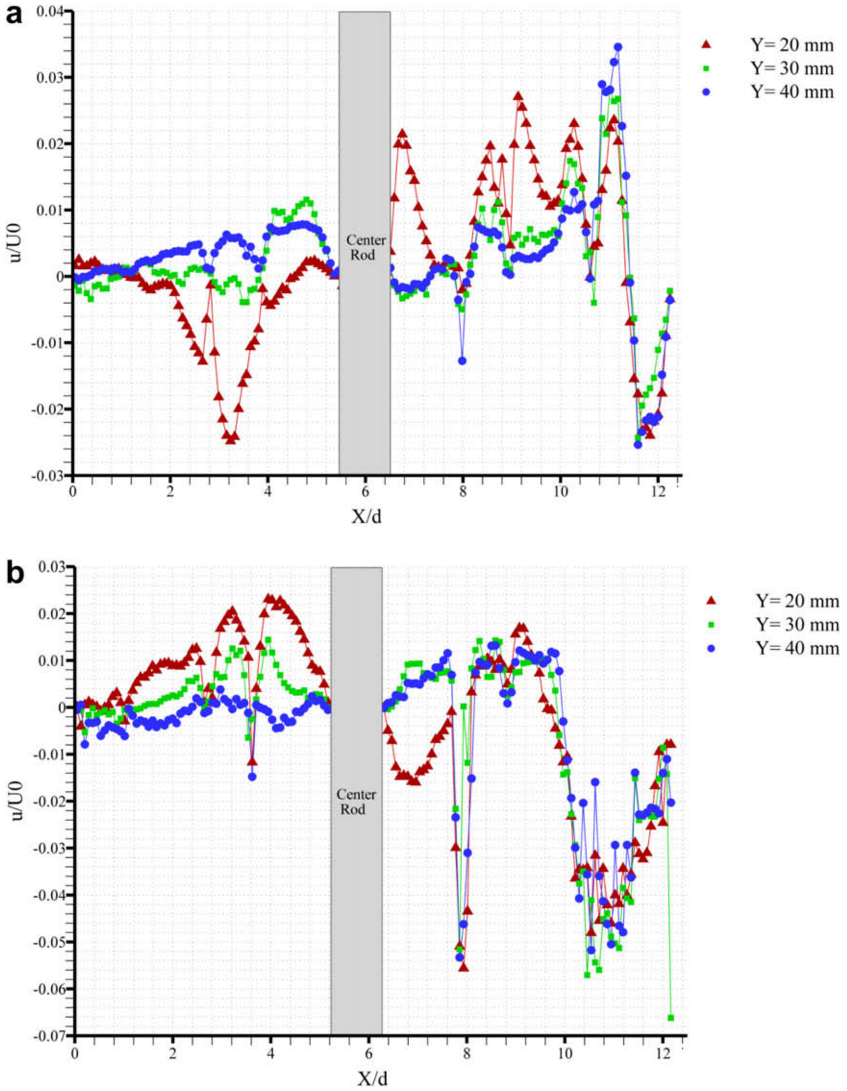

Fig. 9. Normalized *X*-velocity component plot along a lineprobe at different heights of the channel's midplane for a single isothermal inlet jet with (a) $Re_{jet\ 1} = 13{,}400$ and (b) $Re_{jet\ 1} = 4470$.

side of the center rod in the region where one of the two recirculation zones appearing on the left-hand side of the center rod in Fig. 6(a) were located. This is the recirculation zone located closer to the bottom surface of the channel and which covers an area between $Y = 30$ mm and $Y = 20$ mm. In Fig. 8(b), lineprobe of $Y = 40$ mm shows the highest maximum velocity at the center point of the impingement area among the three lineprobes which are shown. On the whole, the maximum velocity at the center point of the impingement area decreases as the jet gets closer to the bottom surface of the channel.

Fig. 9 shows the lineprobes of normalized *X*-velocity component for a single jet impinging into the midplane of the channel with two different Reynolds numbers. Both of the plots show that the magnitude of the *X*-velocity component is rather small compared to the jet's mean velocity and compared to the magnitude of the *Y*-velocity component of that specific case. In Fig. 9(a), the maximum magnitude of the *X*-velocity component, which is less than 4% of the inlet jet's mean velocity, is observed at $Y = 40$ mm. Furthermore, for the case of the lower Reynolds number (Fig. 9(b)), it is seen that the maximum value of the *X*-velocity component happens at $Y = 30$ mm and is less than 7% of the inlet jet's mean velocity. Consequently, the horizontal components of the velocities do not contribute significantly to the whole velocity field and thus will not be discussed further.

Similarly, the turbulence intensities of *Y*-velocity and *X*-velocity components were studied along a lineprobe at three different heights of the channel's midplane for a single impinging jet with two different Reynolds numbers. The results are shown in Figs. 10 and 11 for *Y* and *X* components, respectively. The turbulence intensities play an important role in transferring momentum between the neighboring fluid layers; therefore, they enhance flow mixing.

Figs. 10 and 11 show similar trends; the highest values of turbulence intensities for both *Y*-velocity and *X*-velocity components appear within the region where the jet impinges. There are some other turbulence intensity peaks on both the right- and left-hand side of the center rod in all cases, among which the most prominent one is observed in the area of $X/d = 8–9$ which corresponds well with the recirculation zones and the vorticity patterns that appeared in Figs. 6 and 7. Employing a 2D PIV technique in this experiment, only the 2D flow field on the plane of focus could be captured. In this bundle configuration, the jet injects into the channel and interacts with the center rod located at the impingement plane as well as the rods located in the frontplane and backplane within the area between $X/d = 8–9$ (location of these rods are

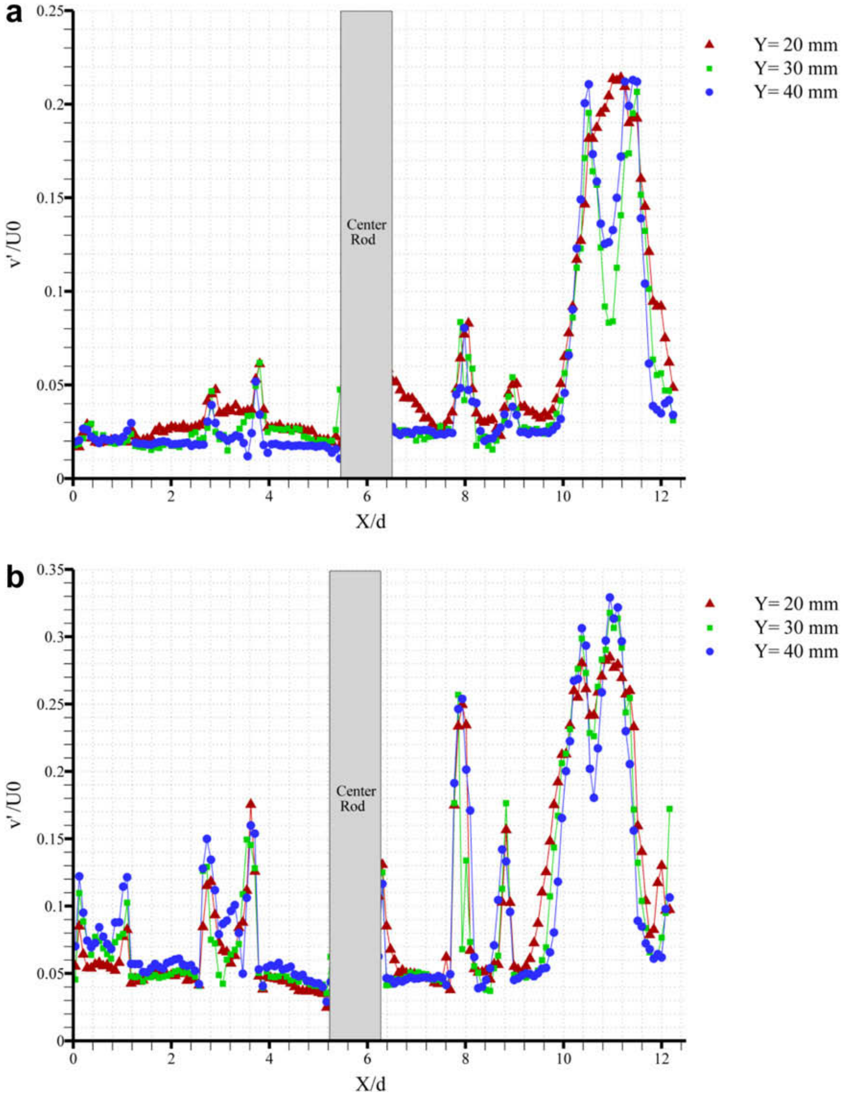

Fig. 10. Turbulence intensity of *Y*-velocity component plot along a lineprobe at different heights of the channel's midplane for a single isothermal inlet jet with (a) $\mathrm{Re}_{\mathrm{jet}\ 1} = 13{,}400$ and (b) $\mathrm{Re}_{\mathrm{jet}\ 1} = 4470$.

clearly seen in Fig. 2). Therefore, some 3D flow patterns and vortical structures are created in those areas between the rods, which affect the flow field in the midplane. The effect of those 3D complex flow structures together with other phenomena happening in the midplane itself such as existence of the main recirculation zone and the shift of streamtraces towards the jet as shown in Fig. 6 in the area of $X/d = 8–9$ results in having some complicated flow structures in that region and having such peaks.

For the higher Reynolds number case, the maximum turbulence intensity of the *Y*-velocity component observed in Fig. 10(a) is almost double the maximum turbulence intensity of the *X*-velocity component seen in Fig. 11(a) which shows the higher contribution of the *Y*-velocity fluctuations in the flow field. On the other hand, the maximum turbulence intensity of the *Y*-velocity component observed in Fig. 10(b) is close to the maximum turbulence intensity of *X*-velocity component seen in Fig. 11(b) which shows the fact that velocity fluctuations in both directions contribute to the flow field to the same extent.

Fig. 12 shows the distribution of the Reynolds shear stresses along a lineprobe at three different heights of the channel's midplane for two cases of single impinging jets with different Reynolds numbers. As seen in Fig. 12, the jet has two peaks of similar magnitude in opposite directions for both Reynolds numbers. Another similarity between the cases is that the magnitude of Reynolds shear stresses goes to zero in the outer region and the center point of the impinging jets. All of these characteristics validate the definition of the Reynolds shear stresses for a standard turbulent jet. Also in both cases, far from the impingement area, the Reynolds shear stresses are zero with some minor fluctuations due to the velocity fluctuations in those areas.

As mentioned previously, in order to visualize the flow behavior throughout the measurement volume, three discrete planes inside the interrogation volume were monitored for the different inlet jet conditions. Fig. 13 compares the *Y*-velocity lineprobes of those three different planes at a specific height of the channel ($Y = 40$ mm) for two cases of single impinging jets with different Reynolds numbers. In each of the plots, the *Y*-velocity magnitude is normalized by the inlet jet's mean velocity obtained from the readings of the flowmeter which is installed upstream of the inlet jet and the length and depth of the measurement volume are normalized by the inlet jet's inner diameter.

In both plots of Fig. 13, the *Y*-velocity lineprobes in the backplane and the frontplane of the measurement volume have much less fluctuation compared to the *Y*-velocity lineprobe of the

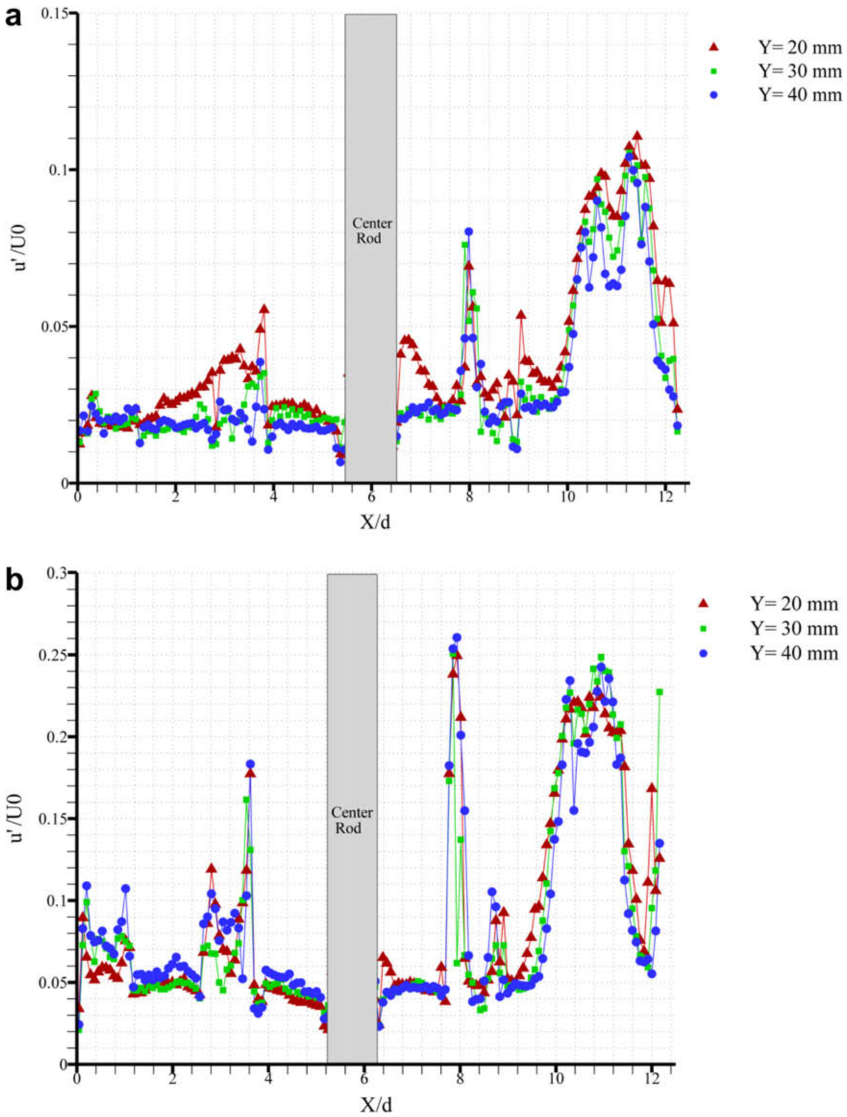

Fig. 11. Turbulence intensity of *X*-velocity component plot along a lineprobe at different heights of the channel's midplane for a single isothermal inlet jet with (a) $\mathrm{Re}_{\mathrm{jet}\ 1} = 13{,}400$ and (b) $\mathrm{Re}_{\mathrm{jet}\ 1} = 4470$.

midplane where the jet is located. Furthermore, in both cases, the jet's *Y*-velocity profile has a parabolic shape with its maximum at the center of the region where the jet impinges. Apart from this region, the *Y*-velocity lineprobe of the midplane behaves similarly to the *Y*-velocity lineprobes of the frontplane and the backplane, where little fluctuation occurs in its velocity.

3.2. Dual jets

In this case, both inlet jets (Inlet Jet 1 and Inlet Jet 2) injected the working fluid into the channel, each with a different Reynolds number. As in the case of the single jets, the time-averaged velocity fields were developed at three different planes within the interrogation volume for each of the inlet jet conditions. Fig. 14 depicts the time-averaged velocity field for one test case, with white streamtraces showing the important features of the flow. Again, the black arrows represent the velocity vectors which are overlaid on a contour map of the *Y*-velocity component.

Contrary to the discontinuity observed in Fig. 6, Fig. 14 shows that both inlet jets velocity profiles were completely captured using the PIV technique. It should also be asserted that in this case the time-averaged velocity field has been presented without any data interpolation, approximation or smoothing.

For both jets in Fig. 14 a well-defined velocity gradient is observed, showing a maximum velocity at the jet's core and decreasing in the horizontal direction. It can also be observed that the streamtraces on the left-hand side of the higher Reynolds number jet and the streamtraces on the right-hand side of the lower Reynolds number jet are shifted towards the jets while the streamtraces on the left-hand side of the lower Reynolds number jet are shifted towards the left-hand side of the interrogation area, which is closer to the channel outlet. The camera lens was not able to capture information to the right-hand side of the higher Reynolds number jet and thus the streamtraces could not be identified in that region. However, if the streamtraces in this section follow the same pattern as the streamtraces of the single jet case, they are expected to be pulled towards the jet. Furthermore, as it is presented in Fig. 14, the higher Reynolds number jet maintains its highest velocity core up to a higher depth of the channel from the inlet jet exit than the lower Reynolds number jet. Most of the above mentioned observations reflect the remarks made about the single jet cases.

Two recirculation zones of different sizes are detected on either side of the center rod; however, the locations of these recirculation

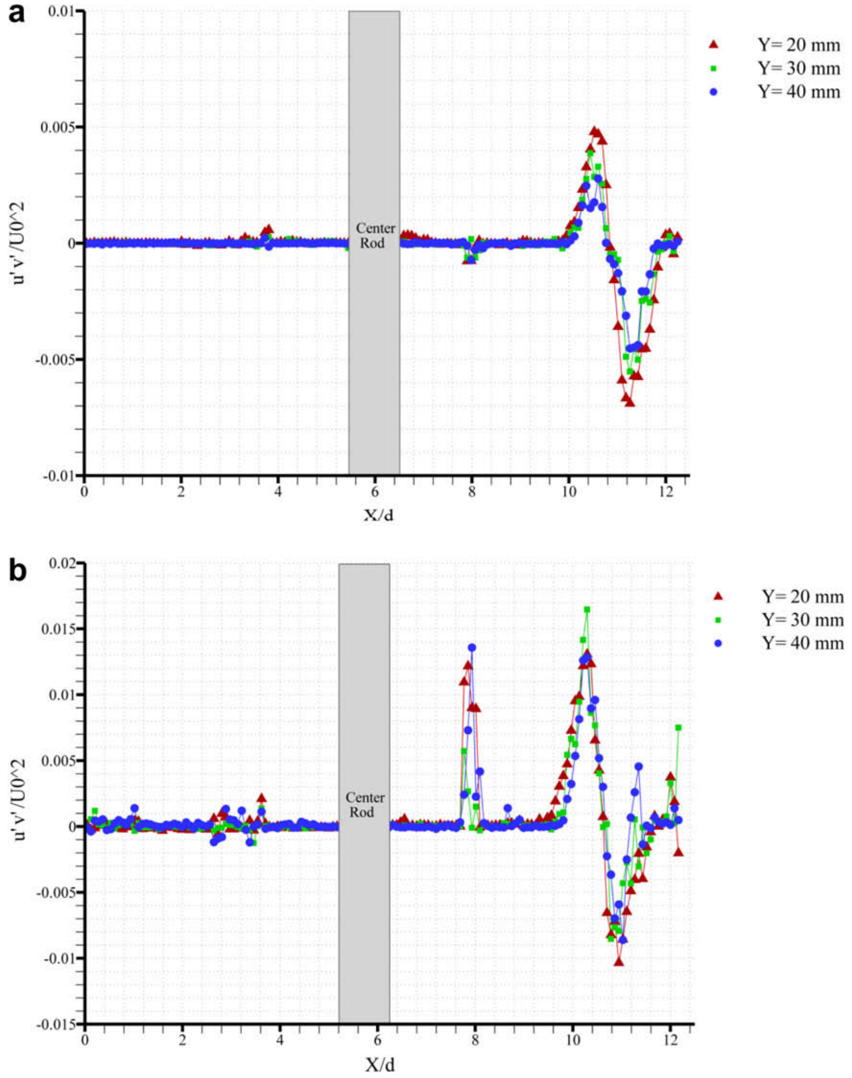

Fig. 12. Normalized Reynolds shear stresses plot along a lineprobe at different heights of the channel's midplane for a single isothermal inlet jet with (a) $Re_{jet\ 1} = 13{,}400$ and (b) $Re_{jet\ 1} = 4470$.

zones differ from one jet to the other. The recirculation zone on the right-hand side of the center rod appears slightly higher and farther from the center rod and is stronger when compared to the left-hand side recirculation zone. These observations resemble those of the single jet except for a few key differences. A brief evaluation of Figs. 14 and 6 indicates that the size of the recirculation zones on the adjacent rod of an impinging jet is directly related to the Reynolds number of the jet. However, no such statement could be made about the dependence of the location of the recirculation zone on the Reynolds number of the jet. As mentioned before, in Fig. 6 the recirculation zone of the single impinging jet with a higher Reynolds number occurs at a lower height and closer to the center rod than the lower Reynolds number case, while in Fig. 14 the recirculation zone adjacent to the higher Reynolds number jet appears at a higher height and farther from the center rod compared to the lower Reynolds number jet. The discrepancy in the location of the recirculation zones between the cases of a single jet and the case of the dual impinging jets may be a result of the interaction between the two jets. In that case, additional dual jet cases must be studied to verify such corresponding relationship.

In Fig. 15, the instantaneous velocity vectors and the vorticity field are shown for the case of dual impinging jets each having a different Reynolds number. As seen in Fig. 15, vortex structures with opposite directions are seen in the outer regions of each impinging jet. As mentioned before, the opposite directions of the vortices are shown by positive and negative values. Similar to the single jet cases, vortex structures have scarcely been identified in the center region of each jet. The magnitude of the vorticity is noticeably higher for the higher Reynolds number jet when compared to the jet with the lower Reynolds number. As before, the presence of the vortices in the outer regions of the jets validates the entrainment of channel flow indicated by the shifted streamtraces toward the jet in Fig. 14.

Additionally, the prediction made about the streamtraces on the right-hand side of the higher Reynolds jet is confirmed by the vortex structures located on that side of the jet, such that the jet is pulling the channel flow towards itself. On the whole, it could be said that the jets entrain some of the channel flow while injecting into the channel. Also it is observed in Fig. 15 that the vorticity patterns in the opposite outer regions of the higher Reynolds jet portrays symmetry, especially in the top part of the jet. On the other hand, the vortex structures are more spread out and non-symmetrical for the lower Reynolds number jet. Furthermore, a number of small vortex structures are observed on the left-hand side of the

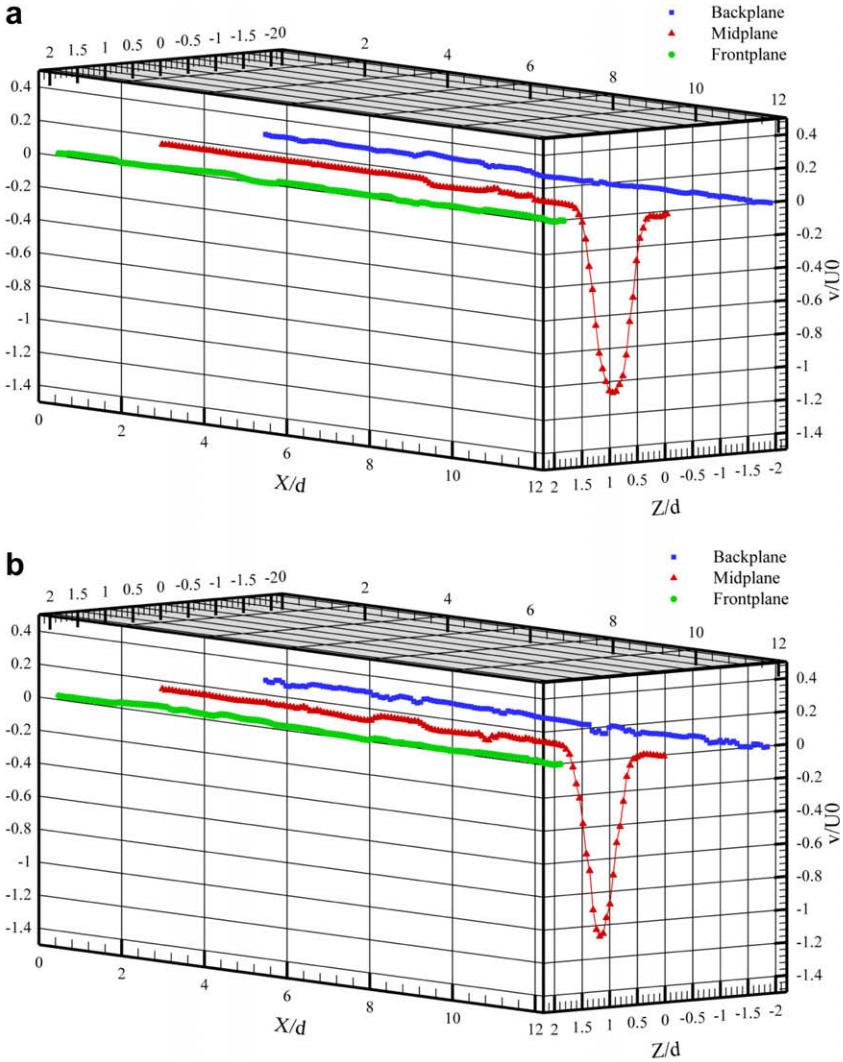

Fig. 13. Normalized Y-velocity component plot along a lineprobe at a constant height of the channel ($Y = 40$ mm) at three different planes (a) $Re_{jet\ 1} = 13{,}400$ and (b) $Re_{jet\ 1} = 4470$.

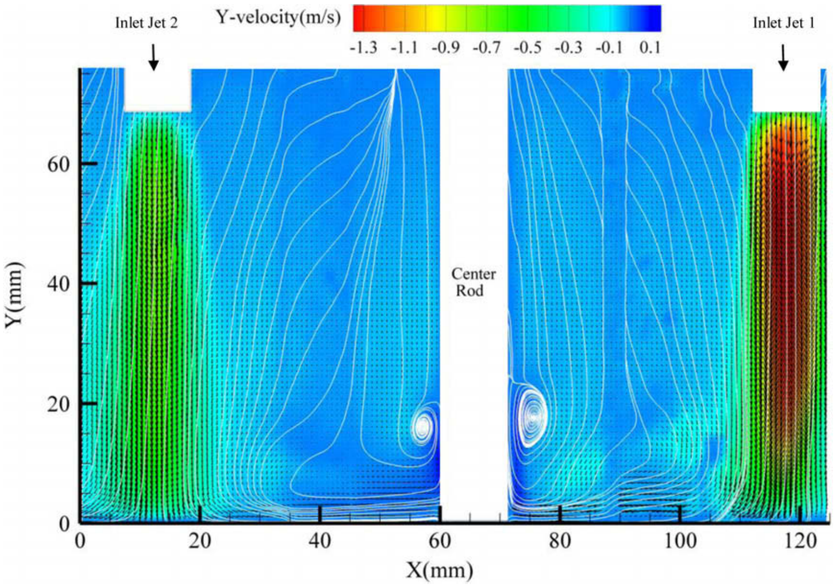

Fig. 14. Time-averaged velocity field, the contour plot of the Y-velocity component and the streamtraces along the vertical midplane for the case of two isothermal inlet jets with different Reynolds numbers: $Re_{jet\ 1} = 11{,}160$ and $Re_{jet\ 2} = 6250$.

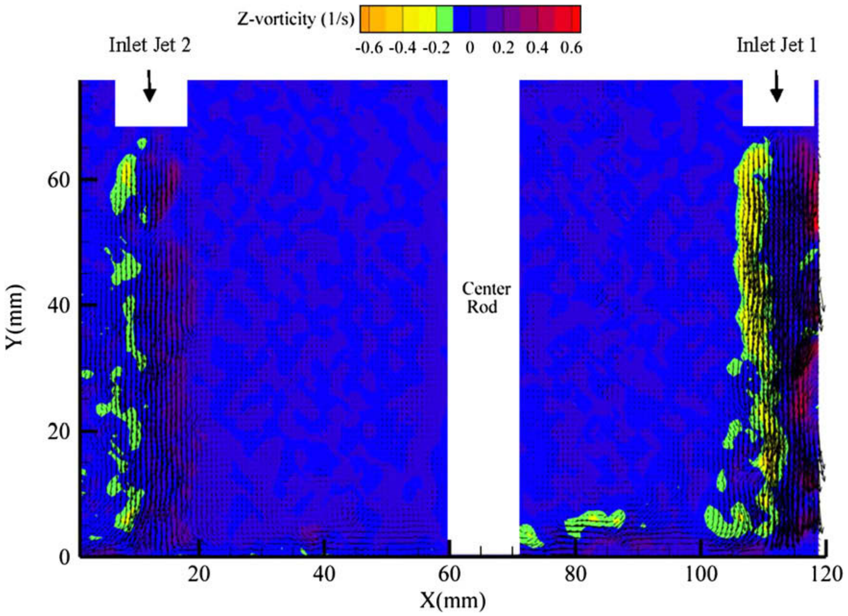

Fig. 15. Instantaneous velocity vectors overlaid on a contour map of *Z*-vorticity along the vertical midplane for the case of two isothermal inlet jets with different Reynolds numbers: $Re_{jet\ 1} = 11{,}160$ and $Re_{jet\ 2} = 6250$.

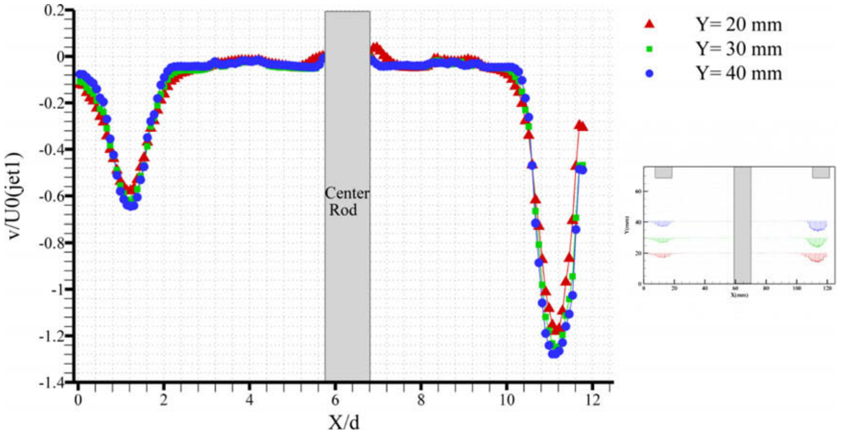

Fig. 16. Normalized *Y*-velocity component plot along a lineprobe at different heights of the channel's midplane for the case of two impinging jets with different Reynolds numbers: $Re_{jet\ 1} = 11{,}160$ and $Re_{jet\ 2} = 6250$.

lower Reynolds jet, which is closer to the channel outlet. These small vortices help to explain why the streamtraces in this region were shifted towards the left-hand side of the picture in Fig. 14.

The lineprobes of the *Y*-velocity component and *X*-velocity component are taken at three different heights of the channel's midplane to help provide a more quantitative understanding of the jet's velocity profile and its evolution. The *Y*-velocity and *X*-velocity components are shown in Figs. 16 and 17, respectively. Here also, the velocity components and horizontal distance are normalized according to the higher Reynolds number jet's mean velocity and the inlet jet's inner diameter, respectively.

In Fig. 16, both jets provide the highest measured velocity at 40 mm above the bottom surface of the channel. A positive velocity is also observed on both sides of the center rod at 20 mm above the bottom surface where the two recirculation zones appear in Fig. 14. As seen in Fig. 16, the lineprobes of $Y = 40$ mm and $Y = 30$ mm for both jets match well with each other in the regions where the jets impinge, while the lineprobe of $Y = 20$ mm shows a slightly reduced maximum velocity at the center of the jets when compared to the other two lineprobes at the same regions. Thus each jet's maximum velocity decreases as it gets closer to the bottom surface of the channel. This difference between the maximum velocity of the lineprobe at $Y = 20$ mm and the other two lineprobes is more apparent for the case of the higher Reynolds number jet.

The normalized lineprobes of the *X*-velocity component for dual impinging jets of different Reynolds numbers are presented in Fig. 17. All of the lineprobes in this figure show that the magnitude of the *X*-velocity component is quite small compared to the higher Reynolds number jet's mean velocity. The maximum magnitude of the *X*-velocity component is less than 4% of the higher Reynolds jet's mean velocity and is located at $Y = 40$ mm. Therefore, the *X*-velocity component in this case similar to the *X*-velocity component in both of the single jet cases does not have a major role in determining the whole velocity field.

One interesting feature observed in Fig. 17 is the two small peaks on either side of the center rod at $Y = 20$ mm. The two peaks correspond well with the two recirculation zones seen in Fig. 14 at each side of the center rod. The reason why one of the peaks has a

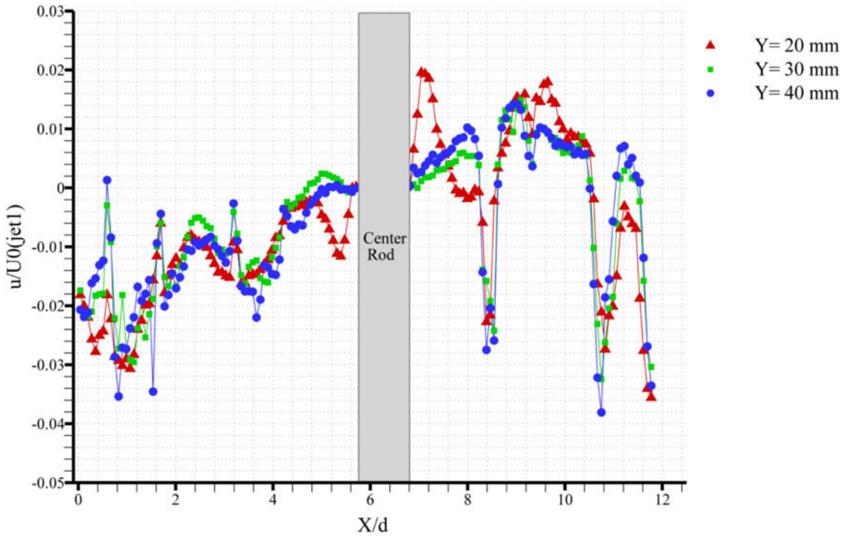

Fig. 17. Normalized *X*-velocity component plot along a lineprobe at different heights of the channel's midplane for the case of two impinging jets with different Reynolds numbers: $Re_{jet\ 1} = 11{,}160$ and $Re_{jet\ 2} = 6250$.

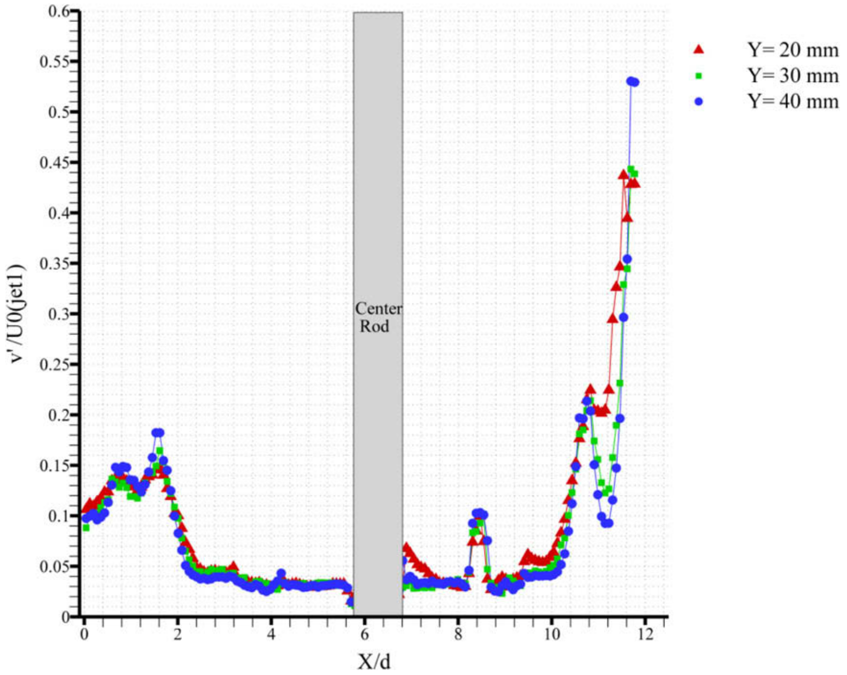

Fig. 18. Turbulence intensity of *Y*-velocity component along a lineprobe at different heights of the channel's midplane for the case of two impinging jets with different Reynolds numbers: $Re_{jet\ 1} = 11{,}160$ and $Re_{jet\ 2} = 6250$.

positive value and the other one has a negative value is that the two recirculation zones of Fig. 14 have opposite directions.

The turbulence intensities of *Y*-velocity and *X*-velocity components were also plotted along a lineprobe at three different heights of the channel's midplane for two impinging jets with two different Reynolds numbers and the results are shown in Figs. 18 and 19, respectively. The camera view could not cover the whole region in the right-hand side area of the first jet, therefore a peculiarity is seen at the lineprobes of the turbulence intensities of *Y*-velocity and *X*-velocity components in Figs. 18 and 19 in that region and a small section of the lineprobe passing through the right-hand side of the higher Reynolds number jet is missing.

Figs. 18 and 19 show the highest values of the turbulence intensities of *Y*-velocity and *X*-velocity components appear within the region where the higher Reynolds jet impinges. Furthermore, there are some other turbulence intensity peaks on the right- and left-hand side of the center rod which corresponds with the recirculation zones and the vorticity patterns that were observed in Figs. 14 and 15. In Figs. 18 and 19, the turbulence intensities of *Y*-velocity and *X*-velocity components drop abruptly at the center of each of the jets for all of the lineprobes. It should be noted that for the higher Reynolds number jet, the maximum of the turbulence intensity of *Y*-velocity is significantly higher than the maximum of the turbulence intensity of *X*-velocity. While for the lower Reynolds number jet, the maximum of the turbulence intensities of *Y*-velocity and *X*-velocity are of the same order.

Fig. 20 shows the distribution of the Reynolds shear stresses along a lineprobe at three different heights of the channel's

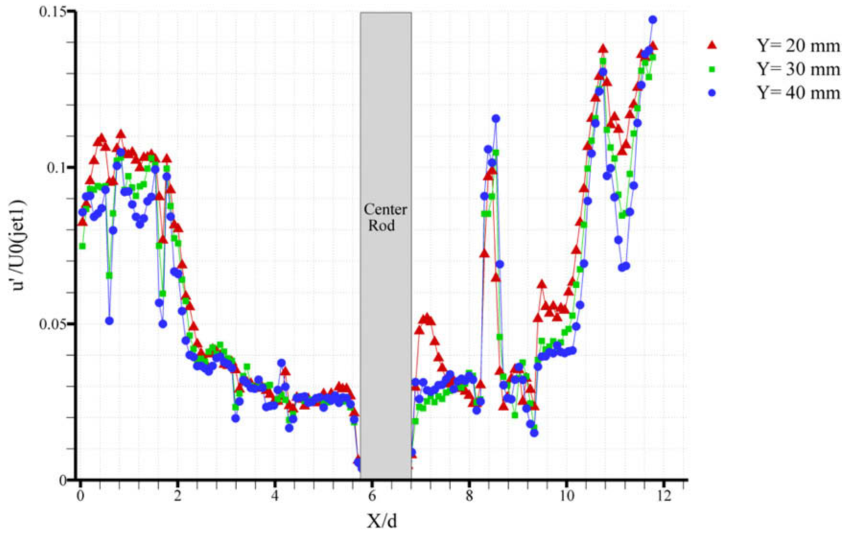

Fig. 19. Turbulence intensity of *X*-velocity component along a lineprobe at different heights of the channel's midplane for the case of two impinging jets with different Reynolds numbers: $Re_{jet\ 1} = 11{,}160$ and $Re_{jet\ 2} = 6250$.

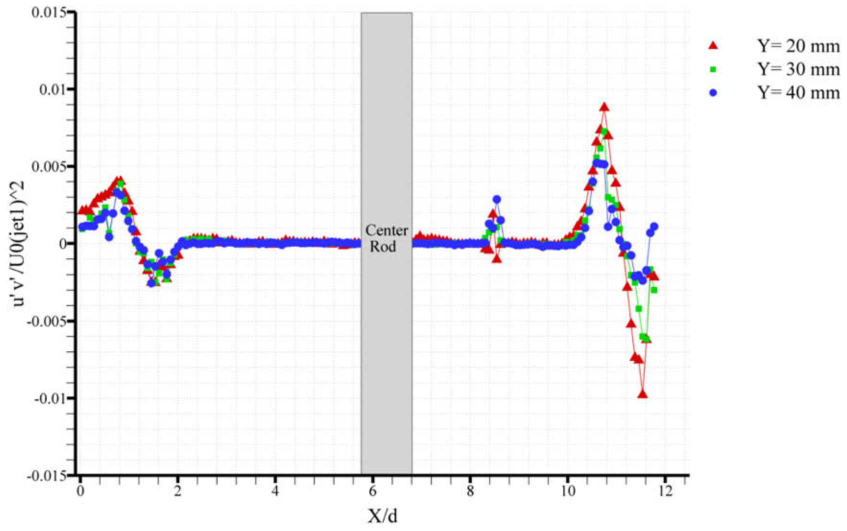

Fig. 20. Normalized Reynolds shear stresses plot along a lineprobe at different heights of the channel's midplane for the case of two impinging jets with different Reynolds numbers: $Re_{jet\ 1} = 11{,}160$ and $Re_{jet\ 2} = 6250$.

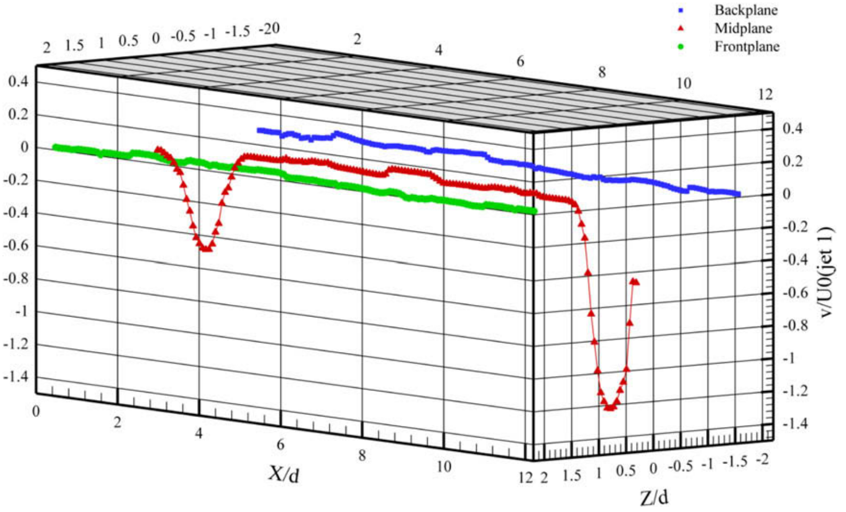

Fig. 21. Normalized *Y*-velocity component plot along a lineprobe at a constant height of the channel ($Y = 40$ mm) at three different planes for the case of two impinging jets with different Reynolds numbers: $Re_{jet\ 1} = 11{,}160$ and $Re_{jet\ 2} = 6250$.

midplane for the case of dual impinging jets with different Reynolds numbers. The Reynolds shear stresses of both jets in Fig. 20 show the same characteristics as the Reynolds shear stresses of each of the impinging jets in Fig. 12. In this case also, the Reynolds shear stresses of both jets have two peaks with slightly different magnitudes in opposite directions and the magnitude of Reynolds shear stresses goes to zero in the outer regions and the center point of each jet. The Reynolds shear stresses reduce to zero (with minor fluctuations) far from the impingement area for both jets. The minor fluctuations in the Reynolds shear stresses far from the jets could be due to the minor velocity fluctuations observed in those areas. However, the Reynolds shear stresses on the left-hand side of the lower Reynolds number jet do not approach zero which could be because of the fact that this inlet jet is located closer to the outlet of the channel leading to higher velocity fluctuations in that area.

In this case also, to visualize the flow behavior within the measurement volume, data were taken at three discrete planes throughout the interrogation volume for different inlet jets' Reynolds numbers. Fig. 21 compares the Y-velocity lineprobes of those three different planes at a specific height of the channel ($Y = 40$ mm) for two isothermal jets impinging into the channel's midplane with two different Reynolds numbers. Here again, the results are normalized in the same way as previously explained for Fig. 13.

Fig. 21 demonstrates that the Y-velocity lineprobes in the backplane and the frontplane of the measurement volume do not oscillate to the same extent as the Y-velocity lineprobe of the midplane. In fact, for both jets, the jets' Y-velocity profiles have a parabolic shape with their maximum value at the center of the region where the jets impinge. Away from this region the Y-velocity lineprobe behaves much more like the Y-velocity lineprobes of the frontplane and the backplane, lacking abrupt variations. These results strongly agree with the conclusion made about Fig. 13 for the two cases of a single isothermal jet with different Reynolds numbers.

4. Conclusions

In this investigation, the mixing of impinging jet flows of various Reynolds numbers into a rectangular channel containing a staggered rod bundle has been studied experimentally through the use of 2D PIV and MIR techniques. The experiment included both single and dual jet flows over a Reynolds number range of 4470–13,400, with data obtained at three separate planes within the interrogation volume. For each case, the time-averaged velocity fields and the vorticity fields of the instantaneous velocity fields were obtained for the investigated flow conditions. Furthermore, the lineprobes of different flow statistics were obtained at three different heights of the channel to study the jet flow evolution in the channel. The results show that using PIV techniques in a Matched-Index of Refraction facility enabled the study of the flow field characteristics in regions within the rod bundle which are normally visually obstructed.

The time-averaged velocity fields for the single jet cases identify the presence of one primary recirculation zone located close to the center rod on the impingement side. The size of this recirculation zone varies directly with the magnitude of the jet's Reynolds number. The time-averaged velocity field of the dual impinging jets confirms the presence of a key recirculation zone at each side of the center rod. The size of each recirculation zone depends on the corresponding jet's Reynolds number. The higher the Reynolds number of the jet is, the larger the size of the major recirculation zone that forms near the center rod is. However, no such conclusion can be made about the location where the recirculation zone appears. It could only be said that the position in which the main recirculation zone happens varies as the jets' Reynolds number changes.

Studying the spatial distribution of vorticity confirms streamtrace observations where flow was shifted towards the jets due to strong vorticity structures found in the outer regions of each impinging jet. This verifies the fact that the jet entrains some of the channel flow in its outer regions. However, it is found that less mixing occurs in the center of the jets than in the outer regions. In addition to that, in all of the cases, several smaller vorticity patterns appear throughout the interrogation area.

Comparing the lineprobes of the Y-velocity component and X-velocity component at different heights of the channel shows that the X-velocity component has a much less significant contribution towards the calculation of the mean velocity compared to Y-velocity component. Also, the lineprobes of the Y-velocity component show that the jet's velocity – especially at its core – decreases as it gets closer to the channel's bottom surface.

By analyzing the lineprobes of the turbulence intensities of Y-velocity and X-velocity components and the Reynolds shear stresses at different heights of the channel it was found for nearly all the cases that the highest values appear in the regions where the jet impinges. Particularly, for the higher Reynolds number jets, the maximum turbulence intensity of Y-velocity component is significantly higher than the maximum turbulence intensity of X-velocity component. While, for the lower Reynolds number jets, the values of maximum turbulence intensities of Y-velocity and X-velocity components are relatively close to each other.

The lineprobes of the Y-velocity were taken at the same height at three different planes inside the rod bundle. They show that the major velocity fluctuations happen in the impingement plane for all cases, while there only exist minor velocity fluctuations in the other two planes.

This study has indicated the presence of one key recirculation zone near the closest rod to each jet. The combination of these recirculation zones, the vorticity patterns at the outer regions of the jets, the smaller vortex structures found throughout the interrogation area, and the high values of turbulent intensities and Reynolds shear stresses in the jets' impingement area, all aid in the enhancement of mixing within the channel.

The data presented in this study could serve as a benchmark for validation of the CFD codes used to simulate the lower plenum flows and their mixing. The complexity of the behavior seen in these regions requires additional investigation to properly characterize the behavior of the thermal jets and their mixing properties.

References

[1] Available from: <http://nuclear.energy.gov/genIV/neGenIV4.html>.

[2] C.Dup. Donaldson, R.S. Snedeker, A study of free jet impingement: Part 1. Mean properties of free and impinging jets, J. Fluid Mech. 45 (1971) 281–319.

[3] C.Dup. Donaldson, R.S. Snedeker, D.P. Margolis, A study of free jet impingement: Part 2. Free jet turbulent structure and impingement heat transfer, J. Fluid Mech. 45 (1971) 477–512.

[4] C.C. Landreth, R.J. Adrian, Impingement of a low Reynolds number turbulent circular jet onto a flat plate at normal incidence, Exp. Fluids 9 (1990) 74–84.

[5] D. Cooper, D.C. Jackson, B.E. Launder, G.X. Liao, Impinging jet studies for turbulence model assessment-I. Flow-field experiments, Int. J. Heat Mass Transfer 36 (1993) 2675–2684.

[6] K. Nishino, M. Samada, K. Kasuya, K. Torii, Turbulence statistics in the stagnation region of an axisymmetric impinging jet flow, Int. J. Heat Fluid Flow 17 (1996) 193–201.

[7] J. Sakakibara, K. Hishida, M. Maeda, Vortex structure and heat transfer in the stagnation region of an impinging plane jet (simultaneous measurements of velocity and temperature fields by digital particle image velocimetry and laser-induced fluorescence), Int. J. Heat Mass Transfer 40 (1997) 3163–3176.

[8] J. Mi, D.S. Nobes, G.J. Nathan, Influence of jet exit conditions on the passive scalar field of an axisymmetric free jet, J. Fluid Mech. 432 (2001) 91–125.

[9] S.V. Alekseenko, A.V. Bilsky, V.M. Dulin, D.M. Markovich, Experimental study of an impinging jet with different swirl rates, Int. J. Heat Fluid Flow 28 (2007) 1340–1359.

[10] A. Abdel-Fattah, Numerical and experimental study of turbulent impinging twin-jet flow, Exp. Therm. Fluid Sci. 31 (2007) 1061–1072.

[11] A.C. Trupp, R.S. Azad, The structure of turbulent flow in triangular array rod bundles, Nucl. Eng. Des. 32 (1975) 47–84.

[12] J.D. Hooper, D.H. Wood, Fully developed rod bundle flow over a large range of Reynolds number, Nucl. Eng. Des. 83 (1984) 31–46.

[13] J.D. Hooper, K. Rehme, Large-scale structural effects in developed turbulent flow through closely-spaced rod arrays, J. Fluid Mech. 145 (1984) 305–337.

[14] K. Rehme, The structure of turbulent flow through rod bundles, Nucl. Eng. Des. 99 (1987) 141–154.

[15] K. Renksizbulut, G.I. Hadaller, An experimental study of turbulent flow through a square_array rod bundle, Nucl. Eng. Des. 91 (1986) 41–55.

[16] L.D. Smith III, M.E. Conner, B. Liu, M.B. Dzodzo, D.V. Paramanov, D.E. Beasley, H.M. Langford, M.V. Holloway, Benchmarking computational fluid dynamics for application to PWR fuel, in: Proceedings of the 10th International Conference on Nuclear Engineering, Arlington, VA, 2002, pp. 823–830.

[17] S.K. Chang, S.K. Moon, W.P. Baek, Y.D. Choi, Phenomenological investigations on the turbulent flow structures in a rod bundle with mixing devices, Nucl. Eng. Des. 238 (2007) 600–609.

[18] F.J.S. Velasco, C. López del Prá, L.E. Herranz, Expansion of a radial jet from a guillotine tube breach in a shell-and-tube heat exchanger, Exp. Therm. Fluid Sci. 32 (2007) 947–961.

[19] D.M. McEligot, G.E. McCreery, Scaling studies and conceptual experiment designs for NGNP CFD assessment, INEEL/EXT-04-02502, Idaho National Engineering and Environmental Laboratory Bechtel BWXT Idaho, LLC, November 2004.

[20] G.E. McCreery, K.G. Condie, Experimental modeling of VHTR plenum flows during normal operation and pressurized conduction cooldown, INL/EXT-06-11760, Idaho National Laboratory, Idaho Falls, Idaho 83415, September 2006.

[21] E. Hecht, Optics, fourth ed., Addison-Wesley, San Francisco, CA, 2002. pp. 92–95.

[22] M. Raffle, C. Willert, J. Kompenhans, Particle Image Velocimetry – A Practical Guide, Springer, Berlin, Heidelberg, Germany, 1998. pp. 13–16.

[23] R.J. Adrian, Particle-imaging techniques for experimental fluid mechanics, Annu. Rev. Fluid Mech. 23 (1991) 261–304.

[24] Y.A. Hassan, T.K. Blanchat, C.H. Seeley Jr., R.E. Canaan, Simultaneous velocity measurements of both components of two phase flow using particle image velocimetry, Int. J. Multiphase Flow 18 (1992) 371–395.

[25] Y.A. Hassan, T.K. Blanchat, C.H. Seeley Jr., PIV flow visualization using particle tracking techniques, Meas. Sci. Technol. 3 (1992) 633–642.

[26] R.J. Adrian, Twenty years of particle image velocimetry, Exp. Fluids 39 (2005) 159–169.

[27] K.C. Kim, Y.U. Min, S.J. Oh, N.H. An, B. Seoudi, H.H. Chun, I. Lee, Time-resolved PIV investigations on the unsteadiness of a low Reynolds number confined jet, J. Vis. 10 (2007) 367–379.

[28] M. Stanislas, K. Okamoto, C.J. Kähler, J. Westerweel, F. Scarano, Main results of the third international PIV challenge, Exp. Fluids 45 (2008) 27–71.

[29] Available from: <http://piv.vsj.or.jp/piv/image3d/image301.html>.

[30] N. Amini, E.E. Dominguez-Ontiveros, C.E. Esterada-Peraz, S.D. Fortenberry, Y.A. Hassan, PIV Measurements of jet flow mixing in the vicinity of rod bundles using matched-index of refraction, in: Proceedings of the 16th International Conference on Nuclear Engineering, Orlando, FL, ICONE16-48853, 2008, pp. 1–5.